Journal of Nuclear Materials 404 (2010) 97–108

Contents lists available at ScienceDirect

Journal of Nuclear Materials

journal homepage: www.elsevier.com/locate/jnucmat

In situ oxidation of zirconium binary alloys by environmental SEM and analysis by AFM, FIB, and TEM

C. Proff [a], S. Abolhassani [a,*], M.M. Dadras [b], C. Lemaignan [c]

[a] Paul Scherrer Institute, 5232 Villigen-PSI, Switzerland
[b] Service of Microscopy and Nanoscopy, IMT, University of Neuchâtel, Jaquet-Droz, 1, 2007 Neuchâtel, Switzerland
[c] CEA Grenoble, 17 Rue de Martyrs, 38054 Grenoble Cedex 9, France

ARTICLE INFO

Article history:
Received 15 December 2009
Accepted 13 May 2010

ABSTRACT

Binary Zr-alloys containing 1%Fe and 1% Ni (large precipitates) and 1% Cr and 0.6% Nb (small precipitates), as well as a pure Zr sample were exposed in situ at 130 Pa water vapour pressure at 415 °C in an environmental SEM. The surface topography and composition of each sample was characterised before in situ experiments, during and after oxidation. After oxidation the surface was characterised by SEM and EDS, AFM and TEM combined with EDS. Focused ion beam was used to prepare cross sections of the metal–oxide interface and for the preparation of TEM thin foils.

The oxidation behaviour of precipitates for these alloying elements can be characterised into two large families, those which show a rapid oxidation and those which induce a delayed oxidation in comparison with the Zr-matrix.

At 415 °C after 1 h of oxidation for Zr1%Fe and Zr1%Ni, the formation of protrusions could be detected at the surface, being related to underlying SPP in the oxide. On Zr1%Cr and Zr0.6%Nb unoxidised SPPs were observed in the oxide, close to the metal–oxide interface. These SPPs were, however, oxidised close to the outer surface of the oxide. The surface roughness was increased for all materials after in situ oxidation, however, only for Zr1%Fe and Zr1%Ni protrusions appeared on the surface during oxidation. It was subsequently demonstrated that these latter correspond to the position of SPPs. For Zr1%Fe the surface roughness increased more than in the other materials and on these protrusions small iron oxide crystals have been observed at the surface. These observations confirm that Fe has a different behaviour compared to the other SPP forming elements, and it diffuses out to the free surface of the material.

These alloying elements being the constituents of the commercial alloys (Fe and Cr for Zircaloy-4; Fe, Cr and Ni for Zircaloy-2 and Nb for all Nb-containing alloys), this study allows to separate their individual influence and can allow a subsequent comparison to the behaviour of those more complex alloys.

1. Introduction

The corrosion resistance of commercial alloys of the Zircaloy group in water and steam is influenced by the presence of intermetallic secondary phase particles (SPP). The precipitates are known to play an important role on the resistance of the material to corrosion through anodic protection [1,2]. For a better understanding of the influence of SPPs on the corrosion properties, several studies of binary zirconium alloys have been conducted in the past [3–14]. So far there is no published study, showing the behaviour of alloying elements at a microscopic level during the initial stages of oxidation, except for the study of a standard Zircaloy-4 in situ at 700 °C by Abolhassani et al. [15].

Zirconium and its alloys oxidise spontaneously at room temperature and develop a self-healing layer of adhesive and protective oxide. At high temperatures and in the presence of water vapour the oxidation continues and a uniform oxide layer forms.

The kinetics of the oxide thickness growth on zirconium is controlled by the migration of oxygen ions through the existing oxide layer and the interaction with the metal at the metal–oxide interface [16]. Depending on the composition and the oxidation conditions, three crystallographic structures have been reported for the ZrO_2 layer: monoclinic, tetragonal and in rare cases cubic zirconia [17]. The ratio of different oxide phases has been shown to be dependent on the material composition and on corrosion conditions (temperature, chemistry, etc.) [18,19]. The presence of stresses in the oxide close to the metal–oxide interface is known [20]. Those compressive stresses in the oxide at the metal–oxide interface have been assumed to exert a stabilizing effect on the tetragonal oxide [21], as the tetragonal oxide content is decreasing together with the stress levels.

The oxidation rate is known to depend on the composition of the material and follows a cubic rate law at the early stages,

---

* Corresponding author. Tel.: +41 56 310 2191; fax: +41 56 310 2203.
E-mail address: sousan.abolhassani@psi.ch (S. Abolhassani).

0022-3115/$ - see front matter © 2010 Elsevier B.V. All rights reserved.
doi:10.1016/j.jnucmat.2010.05.012

changing after a so-called transition period to a linear oxidation rate [22]. For certain alloys cyclic cubic and linear rate laws have been reported [23]. Commercial Zr-alloys Fe is used in higher concentrations than the other alloying elements forming SPP [24], as this resulted in better corrosion resistance in the reactor.

Although many studies have been conducted, certain aspects of the oxidation are still not clear. For example the cause for the change in oxidation rate is still not well understood. If oxygen migration were the only rate determining parameter throughout the process, the rate of oxidation should be related to the thickness of the oxide layer and reduce with time. This relationship is only observed for the pre-transition stage, for the post-transition regime a linear oxidation rate is found, which leads to further continuous oxidation of the material. For these changes of oxidation rates, faster routes for oxygen transport to the interface are necessary. Pores and cracks perpendicular to the interface might facilitate the oxygen access to the metal–oxide interface [25]. Studies performed by scanning electron microscopy (SEM) [25] and transmission electron microscopy (TEM) have shown the presence of cracks in the oxide layer [26–29]. The cause of their formation has not yet been identified up to now.

To our knowledge till present the use of TEM for the study of SPPs in binary zirconium alloys has only been reported by Pecheur [12], who studied Zr1%Nb. No environmental scanning electron microscopy (ESEM) or atomic force microscopy (AFM) study has been reported for binary zirconium alloys.

In order to better understand the role of SPP and the influence of the different alloying elements on the oxidation mechanism, an in situ analysis by ESEM has been performed. The analysis of the surface by AFM before and after oxidation as well as the examination of the material by SEM, energy dispersive X-ray spectroscopy (EDS) and TEM allows a well-defined structural characterisation. Focused ion beam (FIB) method was used to provide site specific TEM samples.

2. Experimental procedure

2.1. Materials

Binary zirconium alloys from a previous study [4] were selected for this examination, their composition and their average SPP size are given in Table 1. The thermal treatment of the material was reported to result in a cumulative annealing parameter of about $\Sigma A = 1.3 \times 10^{-10}$ h with $\Sigma A = \Sigma t \exp -40{,}000/T$, T temperature in K, t the time in hours. This was followed by a stay in the autoclave under 0.1 MPa at 415 °C for 3 days [4]. The oxide scale on those samples, obtained from the autoclave oxidation, has been examined by electrochemical impedance spectrometry [4], metallography, AFM and SEM/EDS in previous studies [30]. The average SPP size of each alloy has been determined in the present study on electropolished TEM specimens. Fe and Ni bearing alloys have much larger SPPs than the Cr and Nb-bearing alloys. The reasons for these differences are explained in [4].

For each sample, a piece (3 mm × 3.5 mm) was cut from the material and the surface was polished down to 1 μm (diamond diameter) with neutral polishing suspensions. The material was ultrasonically cleaned in acetone and ethanol in order to remove all the traces of the polishing suspensions. Three micro-hardness indents were produced on the surface, in order to have reference points for the accurate observation of the same region at different stages of the study.

2.2. Analytical methods and instrumentation

The characterisation procedures and the experimental steps applied to all samples were the following:

1. Atomic force microscopy (polished surface)
2. Scanning electron microscopy (polished surface)
3. Environmental SEM in situ oxidation experiment
4. Scanning electron microscopy (oxidised surface)
5. Atomic force microscopy (oxidised surface)
6. Further scanning electron microscopy/EDS and focused ion beam
7. Transmission electron microscopy

2.3. AFM measurements

AFM of the surface before and after oxidation is used to reveal the change in surface topography during oxidation [15,31]. As the height resolution of the AFM is fully capable of detecting height differences on the sample in the range of nanometers [32], this method is well suited to reveal changes in surface topography after oxidation.

The surface topography of the polished surface was examined by AFM (Digital Instrument Nanoscope IIIa with a silicon tip used in tapping mode at ambient temperature) in order to have a reference for comparison after oxidation. The roughness (quadratic mean of the roughness) of the regions scanned (5 × 5 μm) was determined by averaging the data of at least 5 surface scans with a resolution of 254 × 254 data points.

2.4. ESEM oxidation conditions

The in situ oxidation experiments were performed in a Philips XL30 ESEM–FEG (Field Emission Gun) equipped with an EDS (from EDAX–AMETEK, Inc.). The instrument was operated in ESEM mode. The water vapour pressure was 130 Pa in the specimen chamber. The sample was heated at the maximum possible heating rate of 3.9 °C/s, allowing to reach 415 °C in 2 min. The observations started when this temperature was reached ($t = 0$). The material was held for 60 min at 415 °C and subsequently cooled to ambient temperature. The initial cooling rate of the specimen was about 0.8 °C/s from 415 °C. A gas secondary electron (GSE) detector was used for the high temperature observations.

During the in situ oxidation the surface was continuously observed and images were acquired every 5 min on each specific area of the sample.

At 415 °C the EDS could not be used for chemical analysis. The chemical analysis of the surface was therefore performed after cooling the sample.

Table 1
Chemical analysis of the binary alloys (in wppm or wt.%) and average oxide thickness from Barberis et al. [4], average SPP diameter from this study.

Alloy type	Cr/wppm	Fe/wppm	Ni/wppm	O/wppm	Average oxide thickness/μm	Average SPP size/nm (this study)
Zr1%Fe	44	0.99 wt.%	28	720	0.99	261
Zr1%Ni	46	205	1.17 wt.%	755	0.92	252
Zr1%Cr	1.04 wt.%	247	37	760	0.77	35
Zr0.6%Nb	–	–	–	–	–	47
Pure Zr	–	150	–	300	0.63	–

2.5. FIB sections

The transverse sections of the oxide at specific sites were prepared using FIB. This permitted the direct correlation of features in the section with features on the surface. The sections were made perpendicular to the oxide surface. From those transverse sections the oxide thickness and its variation were determined by milling sections at different positions on the sample and polishing the studied face. The large size of the sections obtained and their high number allows to have a good statistics for the observations. The FIB used was an NVision 40 workstation from Zeiss equipped with the INCA EDS system.

The FIB preparation method was used instead of mechanical polishing, as this resulted in a better image quality of the oxide. Coarse sections were made at 30 kV with a 6 nA beam current, decreasing the beam current down to 150 Pa for the final polish of the transverse sections. The NVision 40 was also used for complementary SEM images and chemical analysis.

2.6. TEM investigation of metal–oxide interface

Thin foils were prepared from the metal–oxide interface by FIB and were examined with the TEM. The material was studied on a JEOL 2010 with an acceleration voltage of 200 keV, equipped with an INCA EDS system using a low background Be double-tilt sample holder. Detailed characterisation of SPP structure and oxygen content was performed by TEM using imaging, diffraction and chemical analysis (EDS). All EDS results presented are semi-quantitative.

3. Results

Surface characterisation before in situ oxidation has been performed as described in "*Experimental procedure*" and results after oxidation for all materials are compared with the as polished data. A detailed example of the whole characterisation procedure is given, here only for Zr1%Fe; all other samples were characterised following the same procedure.

3.1. Zr1%Fe

3.1.1. In situ oxidation of Zr1%Fe

The comparison of the images acquired in situ indicated that the first features becoming more pronounced were already visible with the GSE detector before oxidation at room temperature (Fig. 1a). The evolution of the surface is almost complete after 14 min at 415 °C concerning the larger features observable in Fig. 1b, with only few of them appearing after that time (Fig. 1b and c). After 54 min of in situ oxidation small white particles on top of existing features can be observed (Fig. 1c arrows), the cooling process does not lead to significant surface changes (Fig. 1d). The size of the features remained relatively constant throughout the oxidation process. No cracks were observed during the in situ oxidation and during cooling to room temperature.

3.1.2. SEM after oxidation

The mean diameter of the features on the surface was determined to be ~1 μm and the largest feature being 1.8 μm. The given diameters are average diameters for corresponding circular features (Table 2).

3.1.3. AFM after oxidation

The comparison of the surface roughness of the oxidised surface with the roughness of the polished surface confirms a roughening due to the oxidation process. The roughness of the surface increased from 3.9 nm to 21.2 nm after oxidation (Table 2). An example for the direct comparison of the sample surface before and after

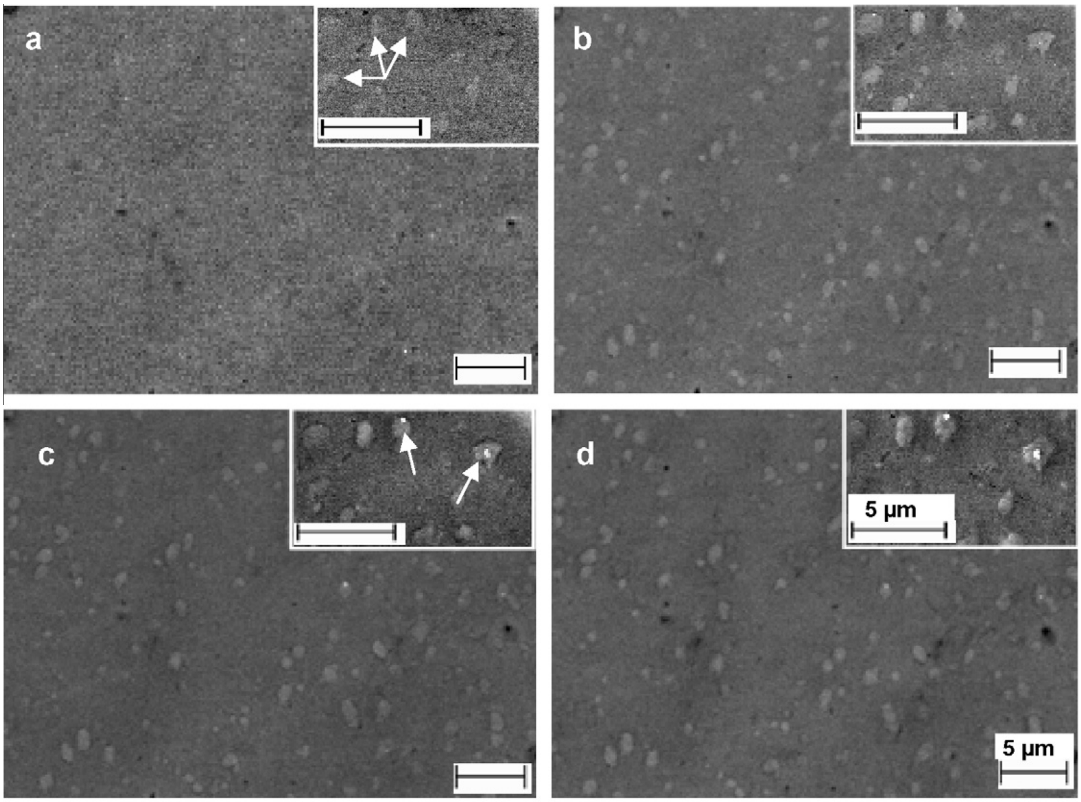

Fig. 1. Sample Zr1%Fe oxidised at 415 °C. The GSE images show the surface (a) as observed before oxidation, (b) in situ after 14 min, (c) in situ after 54 min, and (d) after cooling down to room temperature. Insets show regions imaged at higher resolution.

oxidation is presented in Fig. 2 for Zr1%Fe. The features observed in AFM before oxidation are not linked to the presence of SPP. This can be concluded from the direct comparison of AFM profiles acquired from the same region of the polished and oxidised surface.

The section of the surface profiles on Zr1%Fe (Fig. 2c and d), the location of which is indicated in Fig. 2a and b, reveals the drastical change in surface topography during the first hour of oxidation. Before oxidation no protrusions higher than 4 nm are present in this section, after oxidation the two protrusions observed have a height of 70 nm. The average height of the protrusions after oxidation for 1 h has been measured on 10 AFM profiles to be ~68 nm (Table 2).

3.1.4. SEM and EDS after oxidation

The presence of features appearing during the in situ oxidation at the surface could be subsequently linked to SPP for Zr1%Fe using EDS point analyses and EDS mapping.

In Fig. 3 an example for the characterisation of the features developed during oxidation on the surface of Zr1%Fe is shown. EDS point analyses confirmed the presence of Fe at the positions of features on the surface, while beside them no Fe was detected. The majority of protrusions exhibit only some small particles (Figs. 3b and 2b); while some are densely covered with crystals of up to 100 nm in diameter (Fig. 3c). The EDS analysis of these crystals shows a higher Fe signal in comparison with protrusions without crystals or with finer crystals.

It is already clear from (Figs. 2 and 3) on identical positions of the sample that these SEM features correspond to the AFM protrusions.

The regions with presence of iron according to the EDS map (Fig. 4) were well correlated to the presence of features on the surface. However, some regions with the presence of iron did not exhibit features visible on the surface Therefore to understand the origin of the EDS signal observed at 20 kV acceleration voltage,

Table 2
Parameters of the oxidised samples.

Alloy	Average oxide thickness/μm[a]	RMS polished (5 × 5 μm)/nm	RMS oxidised (5 × 5 μm)/nm	Average height of protrusions/nm[c]	Average diameter of protrusions/μm[c]
Zr1%Fe	0.32 ± 0.11	3.9	21.2[b]	68 ± 15	1.1 ± 0.3
Zr1%Ni	0.41 ± 0.11	5.2	10.3[b]	19 ± 6	0.7 ± 0.5
Zr1%Cr	0.35 ± 0.07	3.8	8.3	Not detectable	
Zr0.6%Nb	0.34 ± 0.09	5.3	9.3		
Pure Zr	0.27 ± 0.05	3.8	11.2	Not detectable	

[a] Average from FIB transverse sections.
[b] Including specific protrusions, RMS: root mean square of roughness.
[c] From 10 sections in AFM profiles.

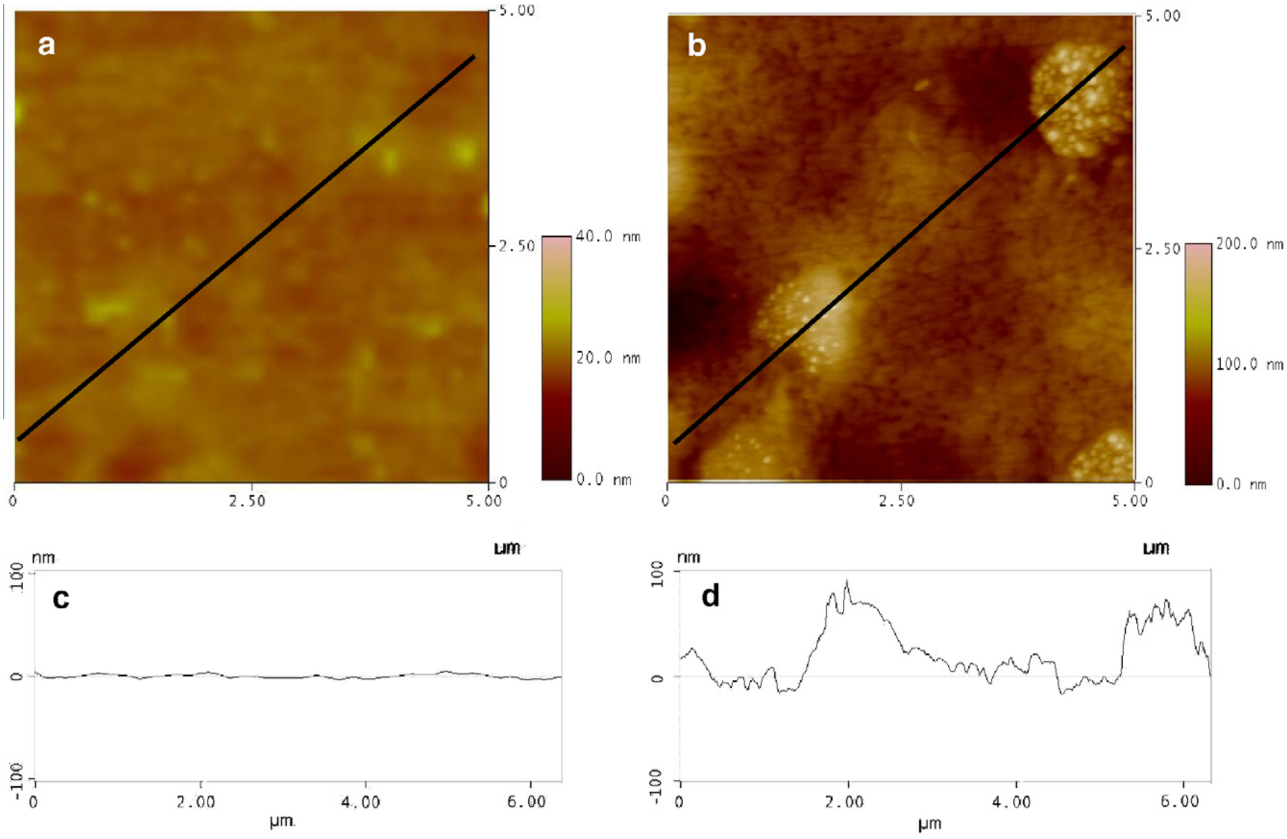

Fig. 2. AFM surface profile on Zr1%Fe (a) polished surface (lower resolution than b) and (b) same region after oxidation. The AFM line profiles c and d represent the sections marked on the surface profiles a and b respectively.

simulations of the electron trajectories in the material were made using CASINO V2.42 [33]. CASINO is a Monte Carlo simulation software for the electron trajectories and generated X-rays in matter.

The penetration of 20 keV electrons into Zr was calculated to be up to 1 μm, electrons having 4% of the original energy in that depth, and the X-ray from the K-line of Fe, Cr and Ni will escape from a maximum depth of 730 nm (90% of overall signal). The oxide thickness on Zr1%Fe is ~320 nm (Table 2), the detected EDS signal can therefore originate from SPPs underneath the oxide layer.

3.1.5. FIB transverse sections

The protrusions on the surface correspond to the underlying SPP as shown for example by the black arrow in the FIB transverse sections and the white arrow on the oxide surface (Fig. 5). The oxide thickness appears to be homogeneous throughout the whole sample. The metal–oxide interface is undulated and the amplitude of the undulation could be increased at the sites of oxidised SPP. This has been also shown in many other sections, linking the features also for the transverse sections to underlying SPPs.

3.1.6. Tem

Further characterisation of the metal–oxide interface was performed by TEM to obtain microstructural and chemical information about the SPP.

A TEM transverse section of oxidised Zr1%Fe is presented in Fig. 6. The oxide layer on the matrix and the thicker oxide at oxidised SPP in contact with the outer surface can be well distinguished in the dark field contrast, arrows mark the metal–oxide interface. A closer examination of the oxide at the oxidised SPP revealed a fine-grained, equiaxed oxide. The neighbouring oxide of

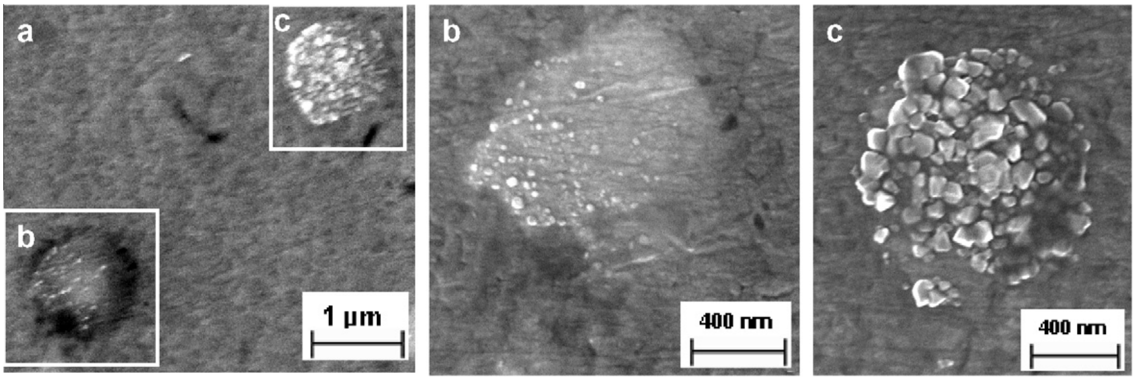

Fig. 3. (a) SEM micrographs of features on the oxidised surface of Zr1%Fe as observed with SE detector. The regions marked (b and c) in (a) are presented at higher magnification in b and c respectively.

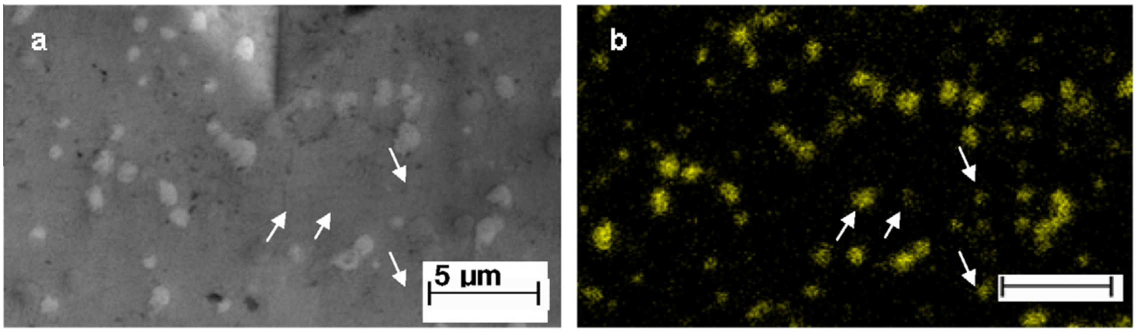

Fig. 4. Zr1%Fe oxidised for 1 h at 415 °C (a) SE image and (b) EDS map of Fe K-edge. Arrows indicate regions with FE signal with no feature at the surface.

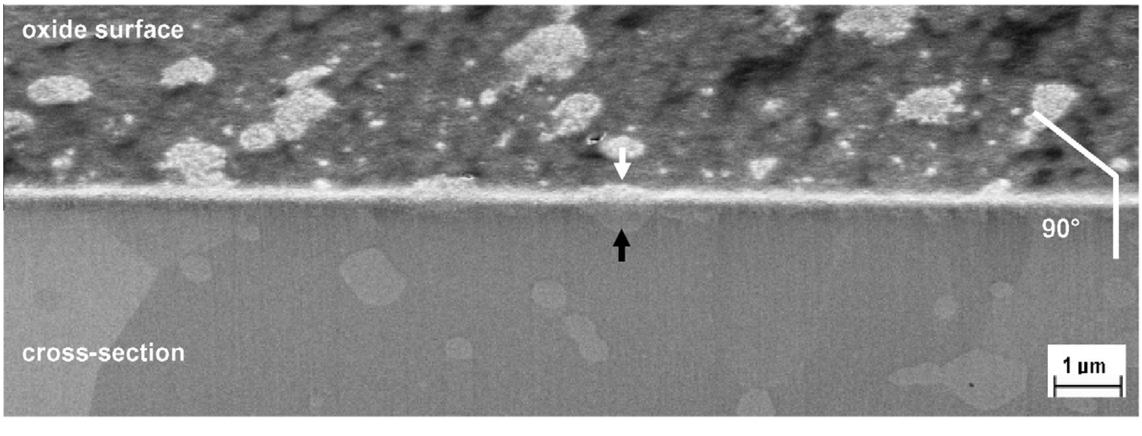

Fig. 5. FIB transverse section of Zr1%Fe sample. One feature on the surface (white arrow) can be directly linked to the underlying SPP (black arrow).

pure zirconia has a columnar structure on the zirconium matrix. In order to examine the nature of crystals formed at the protrusions (as shown in Figs. 2b and 3c) a TEM sample is prepared with special care to protect the outer surface on the site of the crystals. Fig. 6b shows this TEM sample and the crystals present at the surface. TEM diffraction pattern of these oxide crystals (not presented here) showed that they are often single crystals.

Two types of trends can be observed for SPP oxidation:

(a). SPPs in contact with the outer surface. The oxide thickness is higher in those regions and the SPPs are oxidised to a larger extend than the matrix (Fig. 6a).

(b). SPP underneath the original surface. These show an oxidation more or less similar to the zirconium matrix (Fig. 7).

It must be noted that the diffusion of iron to the free oxide surface can be related to the precipitates in contact with the outer surface, however, it cannot be excluded that a certain amount of diffusion takes place also from SPPs below the outer surface.

Those results are also confirmed by the FIB-observation of several tens of SPP, which showed a thicker oxide if initially in contact with the outer surface, leading to the formation of oxide undulations at the metal–oxide interface and similar oxidation like the surrounding matrix if not in contact with the outer surface.

The height of protrusions on the surface caused by oxidised SPP can be measured in Fig. 6a, where a white line is inserted as reference for a flat surface, and also in Fig. 6b. As an example the height of the SPP marked with the line is ~95 nm, which is comparable to the values obtained by AFM (Fig. 2d).

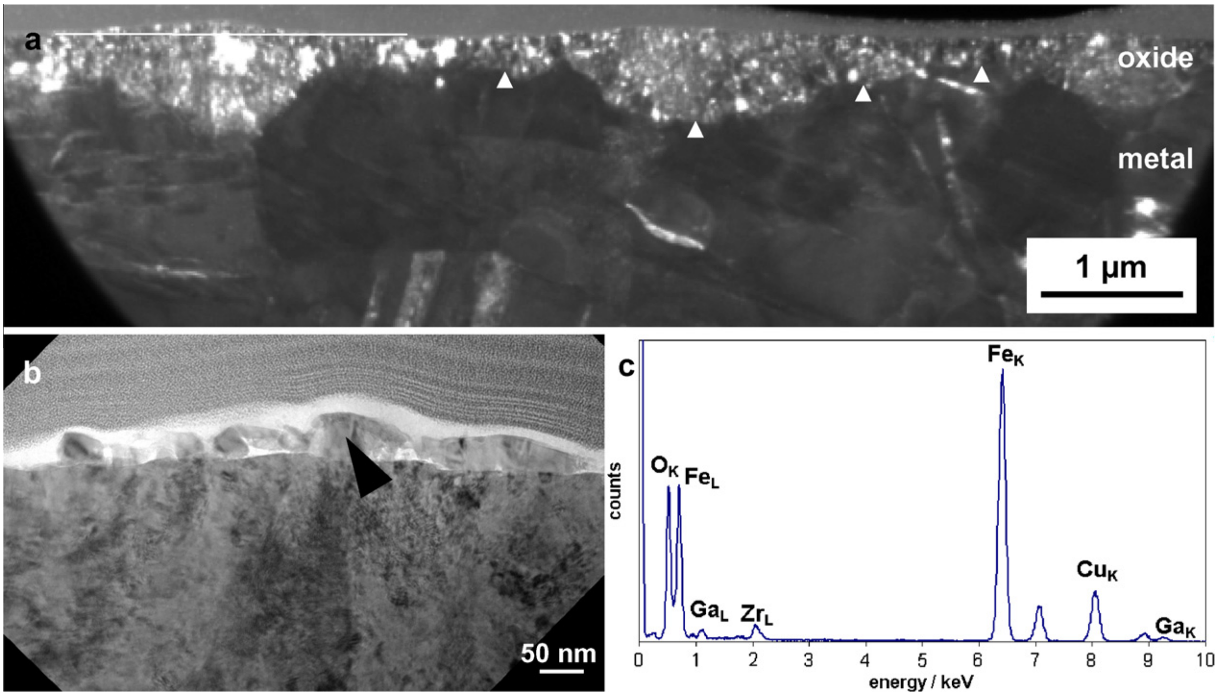

Fig. 6. (a) Dark field contrast of Zr1%Fe. Oxide interface undulations and surface protrusions can be observed at the SPP in contact with the surface. The white arrowheads mark the metal–oxide interface. (b) Bright field contrast showing iron oxide crystals formed on the oxide surface. (c) EDS spectrum of crystals in (Fig. 6b) (location indicated by the black arrowhead). The Cu signal is from the FIB–TEM grid and the gallium signal from implantation during TEM sample preparation.

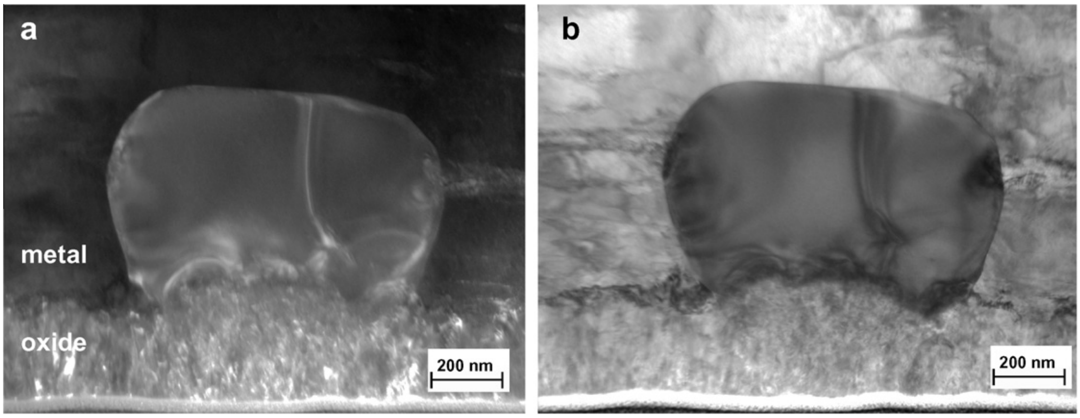

Fig. 7. (a) Dark field contrast and (b) bright field contrast of partially oxidised SPP at the metal–oxide interface of Zr1%Fe.

The EDS analysis of the TEM samples provided the following information:

(a). The crystals formed at the surface consist of almost pure iron oxide. Only small amounts of zirconium and gallium have been detected, the latter being a contamination from the TEM sample preparation process (Fig. 6c).
(b). SPPs in the oxide showed iron and oxygen signals indicating that the precipitates are oxidised (Fe: 10–15 at.%, O: 60 at.%, Zr: 25–30 at.%). Therefore in the case of Zr1%Fe, no metallic SPP was observed in the oxide.
(c). SPPs in the underlying metal near the metal–oxide interface showed an oxygen concentration similar to the surrounding matrix (Fe: 20–30 at.%, O: 10–20 at.%, Zr: 50–60 at.%). In other words the EDS point line scans in the metallic SPPs showed no oxygen enrichment with respect to the zirconium matrix.

3.2. Zr1%Ni

For Zr1%Ni the observations were similar to those for Zr1%Fe. AFM scans on the oxidised surface of Zr1%Ni revealed protrusions with an average height of 19 nm (Table 2).

For Zr1%Ni the formation of metal–oxide interface undulation with higher amplitude has been observed for SPPs in contact with the outer surface. SPPs not in contact with the outer surface exhibit an oxide thickness similar to the surrounding matrix at the metal–oxide interface, they are not preferentially oxidised. The contrast of the interface implied a metallic nature on the metal side and an oxidised on the oxide side.

A TEM transverse section of oxidised Zr1%Ni is presented in Fig. 8. The oxide layer on the matrix and the SPP at the metal–oxide interface and in the metal can be well distinguished in the dark field contrast (Fig. 8a). A closer examination of the oxide at the oxidised SPP revealed a coarse-grained, equiaxed oxide; the grain size is in the same range as the width of the columnar oxide grains on the matrix. The SPP-oxide interface is similar to the matrix–oxide interface.

The EDS analysis of the TEM samples provided the following information:

(a). SPPs in the oxide showed nickel and oxygen signals indicating that the precipitates are oxidised (Ni: 10 at.%, O: 60 at.%, Zr: 30 at.%). In the case of Zr1%Ni, no metallic SPP was observed in the oxide.
(b). The SPPs in the underlying metal showed an oxygen concentration similar to the surrounding matrix (Ni: 25 at.%, O: 10 at.%, Zr: 65 at.%). In other words the EDS point line scans in the metallic SPPs showed no oxygen enrichment with respect to the zirconium matrix.

In the case of this alloy, no Ni diffusion to the outer surface could be detected. This implies if any such phenomenon exists, it is much slower than in the case of the Zr–Fe alloy.

3.3. Zr1%Cr

For Zr1%Cr SPPs were not observed on the surface before oxidation. During the in situ oxidation no changes on the surface other than those typical for the oxidation of the zirconium matrix could be observed. The surface oxide exhibited a coarse-grained aspect with no specific protrusions or cracks, which could be linked to the presence of SPP.

The surface of Zr1%Cr analysed by AFM exhibits no large protrusions but many small oxide grains are observed. The height differences between surface oxide grains are significant enough to make the surface appearing rough. The roughness of the surface increased from 3.8 nm to 8.3 nm after oxidation (Table 2).

The TEM transverse section of oxidised Zr1%Cr is presented in Fig. 9a. Several SPPs can be observed in the oxide layer (Fig. 9b). The undulated metal–oxide interface can be seen (indicated with white dots). The matrix oxide has a columnar grain structure. In an area of approximately 0.3 μm^2 four precipitates can be seen in the oxide. For Zr1%Cr, the SPPs observed in the oxide exhibited a crescent shaped crack towards the outer surface (Fig. 9). Using the integrated EDS signal from EDS spectra, it could be shown, that at the position of the crescents the signal dropped significantly, indicating that the crescents are real cracks in the oxide.

For the measurement of the SPP composition a correction has to be used, as due to the small size of the $ZrCr_2$ SPP, the EDS signal from the surrounding oxide contributes to the signal. Especially for SPP in the oxide, for which the oxygen concentration is of interest, the oxygen content of the SPP is therefore derived from the following calculation:

1. It is assumed that the SPP ($ZrCr_2$) and the surrounding oxide (ZrO_2) are stoichiometric. The amount of Zr in the matrix is calculated using the measured atomic concentration of chromium

$$c(Zr_{matrix}) = c(Zr_{measured}) - 0.5 \cdot c(Cr_{measured}). \quad (1)$$

2. The oxygen content of this matrix is then subtracted from the total oxygen concentration measured (numerator of Eq. (2)). If the numerator is positive, so there is more oxygen than can be present in the matrix around the SPP, the atomic concentration of oxygen in the SPP is calculated with

$$c(O_{SPP}) = \frac{c(O_{measured}) - 2 \cdot c(Zr_{matrix})}{1.5 \cdot c(Cr_{measured}) + \{c(O_{measured}) - 2 \cdot c(Zr_{matrix})\}}. \quad (2)$$

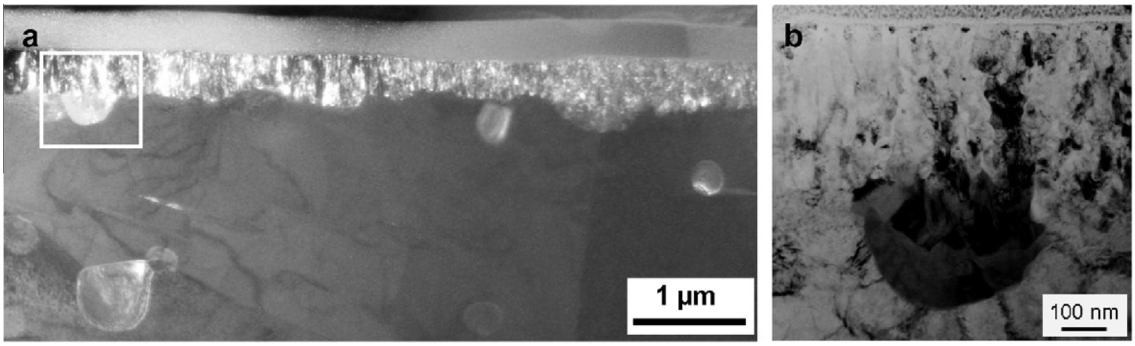

Fig. 8. Dark field image (a) of Zr1%Ni. The precipitate at the metal–oxide interface is partially oxidised. The inset shows a bright field image of a partly oxidised Ni containing precipitate at the metal–oxide interface (b).

The correct quantification at the SPP position was ensured by measuring always the oxide beside the SPP, which should yield an oxygen to zirconium ratio of 2.

The EDS analysis of the SPPs in the oxide provided the following information:

(a) Many SPPs in the oxide exhibit too low oxygen contents to be fully oxidised (0–20 at.% oxygen), while the surrounding matrix was found to be fully oxidised. SPPs within ~150 nm distance of the metal–oxide interface were usually low in oxygen.
(b) Close to the outer surface the SPP oxygen content was observed to be around 60 at.% oxygen, indicating fully oxidised SPPs.

3.4. Zr0.6%Nb

For Zr0.6%Nb no SPP were observed on the surface before oxidation. During the in situ oxidation only changes on the surface typical for the oxidation of the zirconium matrix could be observed. The surface oxide exhibited a coarse-grained aspect with no specific protrusions or cracks, which could be linked to the presence of SPP.

On the surface of Zr0.6%Nb AFM revealed no large protrusions but small oxide grains. The differences in height between the surface oxide grains are significant enough to make the surface appearing rough. The roughness of the surface increased from 5.3 nm to 9.3 nm after oxidation (Table 2).

TEM analysis of Zr0.6%Nb the SPPs in the oxide revealed again a crescent shaped crack above the SPPs towards the outer surface, see Fig. 10. The size of the crescent shaped cracks is correlated to the SPP size. The matrix oxide has a columnar grain structure. As no fixed SPP composition was found on electropolished samples, no direct information about the SPP oxygen content could be obtained using the correction applied for Zr1%Cr. The overall oxygen concentration measured at SPP positions (55–60 at.% oxygen). Therefore these precipitates are not as oxygen deficient as the $ZrCr_2$ SPPs.

3.5. Pure Zr

The results for pure zirconium are shown for comparison to evaluate the influence of the alloying elements on the oxidation behaviour of zirconium.

The surface of pure Zr exhibits no large protrusions. The observed oxide grains are small. The differences in height between the surface oxide grains are significant enough to make the surface appearing rough. The roughness of the surface increased from 3.8 nm to 11.2 nm after oxidation.

For pure Zr the metal–oxide interface was observed in TEM to be undulated (Fig. 11a). The oxide has a columnar grain structure (Fig. 11a and b). Some SPPs due to the iron impurity could be observed, however, they were very rare.

3.6. Comparison of the results from the four binary alloys and the pure Zr

The in situ observations of the oxidation revealed for Zr1%Fe and Zr1%Ni an observable different oxidation of the SPP initially in contact with the outer surface compared to the matrix, resulting in protrusions measurable with AFM at the surface and confirmed on FIB transverse sections and EDS maps of the surface. Their average height is ~70 nm on Zr1%Fe and ~20 nm on Zr1%Ni. In the case of Zr1%Fe small iron oxide crystals of different size were observed on the surface of several SPPs (Fig. 3b and c and Fig. 6b).

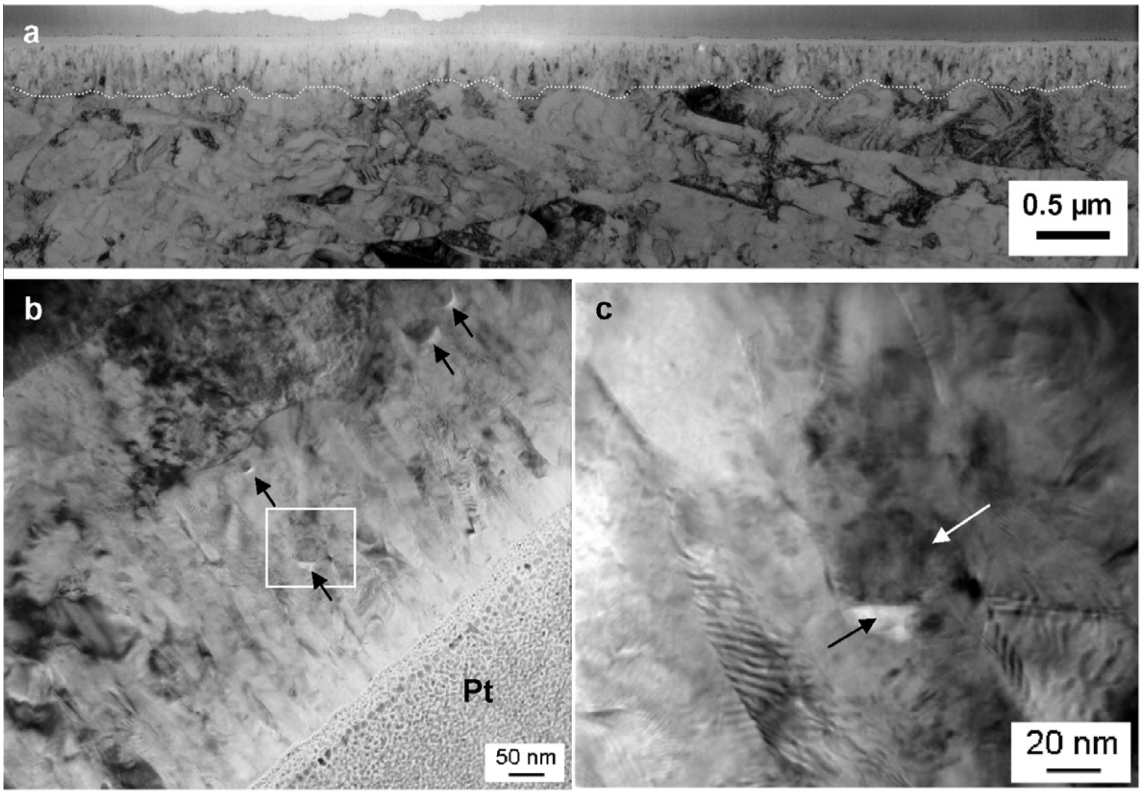

Fig. 9. Bright Field micrographs of Zr1%Cr, (a) overview of the undulated metal–oxide interface. The metal–oxide interface is marked with white dots for clear observation, (b) oxide scale with columnar grain structure and four SPP with crescent shaped cracks, marked with arrows, and (c) SPP at higher magnification from the marked region in (b), showing the crescent shaped crack (black arrow) on top of the SPP (white arrow).

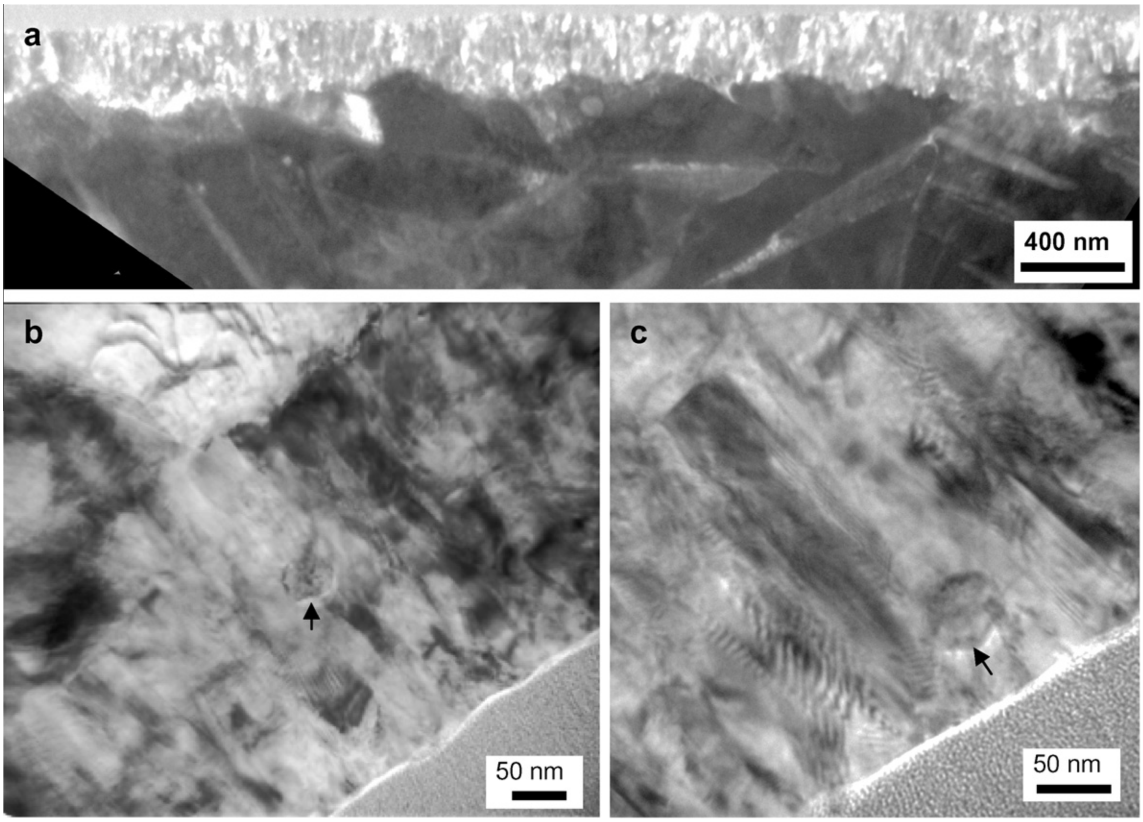

Fig. 10. Micrographs of oxidised Zr0.6%Nb. (a) Dark field contrast of oxide, showing the undulated metal–oxide interface and (b and c) bright field micrographs of SPP in the oxide marked with arrows.

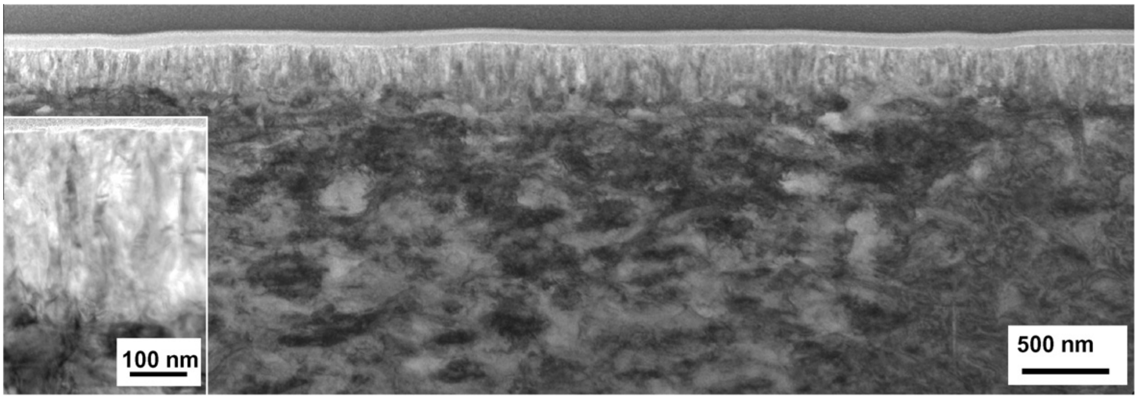

Fig. 11. TEM bright field micrographs of oxidised pure Zr. Overview of oxide scale, showing the undulated metal–oxide interface. Inset at higher magnification showing the columnar oxide.

For Zr1%Cr, Zr0.6%Nb and pure Zr no protrusions could be linked to the SPP present at the surface. The average SPP size of 35 and 47 nm is to be compared to ~250 nm for Zr1%Fe and Zr1%Ni, therefore the change of volume per SPP is much smaller for alloys with smaller SPPs. The average roughness in the case of the Zr1%Fe and Zr1%Ni alloys is in fact the average of protrusions and matrix oxide combined. If we examined the matrix oxide of these two alloys they would reveal a smoother topography as shown in Table 3.

Table 3
surface roughness for matrix oxide of oxidised samples.

Alloy	RMS matrix oxide (700 × 700 nm)/nm
Zr1%Fe	4.5[a]
Zr1%Ni	4.5
Zr1%Cr	4.5
Zr0.6%Nb	5.1
Pure Zr	5.8

[a] From zoomed 5 × 5 μm scans.

All alloys form an oxide scale in the same thickness range, as measured in FIB transverse sections, Zr1%Ni exhibiting the thickest and pure Zr the thinnest oxide scale. The oxidation behaviour of the SPP at the metal–oxide interface can be studied on the FIB transverse sections for Zr1%Fe and Zr1%Ni. For Zr1%Cr and Zr0.6%Nb this is not possible due to the SPP size.

TEM observations showed columnar oxide grains in the matrix oxide for all materials. The oxidation behaviour of the SPP in different alloys differed, Zr_2Ni and Zr_3Fe oxidised similar to the Zr-matrix, if not in contact with the outer surface, while when in contact with the outer surface they showed higher oxide thickness than the surrounding matrix. $ZrCr_2$ showed a delayed oxidation and the Nb containing SPPs were deficient in oxygen compared to the fully oxidised matrix. Both materials showed crescent shaped cracks on the SPP side facing the outer surface.

4. Discussion

The ESEM in situ observations are only providing surface information; however, in combination with complementary ex situ analyses they give a good insight to the processes taking place at the early stage of oxidation.

These can be summarized as follows:

4.1. Change of surface topography

The protrusions observed on the surface of Zr1%Fe and Zr1%Ni were related to the presence of large SPP underneath the surface. The increase in height at these locations could be due to the volume increase difference between the oxidised SPP and oxidised matrix, or due to migration of alloying elements to the free surface and their subsequent oxidation [15]. Both aspects will be discussed below.

In order to quantify the effect of the expansion differences a hypothetical Pilling–Bedworth (P–B) ratio [34] was calculated for the SPP with the equation given by Xu and Gao [35], assuming the formation of ZrO_2 and the respective alloying element oxide (Fe_2O_3, NiO, and Cr_2O_3) with their crystal structure. The P–B ratio gives the ratio between the volume of the formed oxide and the volume of metal consumed forming this oxide.

$$\text{P—B Ratio } (Zr_aM_b) = \frac{\left(\frac{N_{metal}(Zr)}{N_{oxide}(Zr)}\cdot V_{oxide}(Zr)\right) + \left(\frac{N_{metal}(M)}{N_{oxide}(M)}\cdot V_{oxide}(M)\right)}{V_{\mathrm{SPP}}(Zr_aM_b)}$$

where M is the alloying element, $n_{metal}(X)$ the number of atoms of X in unit cell of SPP, $N_{oxide}(X)$ the number of atoms of X in the unit cell of the oxide formed by X and $V_{oxide}(X)$ the volume of the unit cell of the respective oxide.

It was considered, that the pure unconstrained oxide of each of the metals involved is formed (ZrO_2, Cr_2O_3, Fe_2O_3, and NiO). In other words mixed oxides are not considered in our calculations.

For Zr_3Fe a P–B ratio of 1.87 and for Zr_2Ni a P–B ratio of 1.59 was calculated, compared to 1.51 for pure Zr. These values were used to calculate the average height of protrusions for each material for SPPs with diameters of 35 nm and 250 nm. For Zr_3Fe a height of 23 nm was obtained for 250 nm SPPs and a height of 3.1 nm for 35 nm SPPs. Thus the height of protrusions caused by small SPP is in the same range as the roughness of the matrix oxide. Therefore protrusions caused by small SPP cannot be resolved at the surface, even if they are present. For Zr_2Ni the calculation led to a height of 5.6 nm for a 250 nm SPP and a height of 0.75 nm for a 35 nm SPP. Three possibilities are suggested to explain this discrepancy between the experimental results and the calculated heights.

(A) The assumption made about the expansion being a sum of two distinct oxide formations is not valid, another oxide structure is growing.
(B) The possibility that the average height as determined by AFM is an overestimated value, since the smaller protrusions were neglected, due to difficulty in discrimination, as those measured were selected manually from AFM images and the SPP causing the evaluated protrusions were larger than the average SPP.
(C) The height of protrusions is not only due to the P–B ratio but at the same time due to the migration of species to the free surface. This is specially the case of Zr1%Fe alloy, where such crystals have been observed.

For $ZrCr_2$ the same calculations yielded a P–B ratio of 1.75 and a height of 17.9 nm for a 250 nm SPP and a height of 2.4 nm for a 35 nm SPP. Because the SPP are small, the associated protrusions should also have a width of around 35 nm, being not resolvable for the above mentioned reasons. As there is no possibility to do chemical analyses on the small protrusions in AFM, there is no way to tell which ones are caused by oxidised $ZrCr_2$ SPP and which are from the matrix oxide. The same problem applies to the Zr0.6%Nb, however, in this case we have no fixed SPP composition which could have been used to derive a P–B ratio for the SPP.

From the in situ observation and the occurrence of SPP-like features at the very early stages of oxidation (Fig. 1a and b), it can be concluded that the oxidation at the surface takes place simultaneously for the matrix and the SPP. Once the SPP in contact with the surface were all oxidised the number of features at the surface did not increase any further. Moreover, in the case of Zr1%Fe a rapid diffusion of the alloying element to the free surface is also observed.

The different oxidation behaviour of the precipitates could be at the origin of the development of nodules on the surface of the claddings, as it has been observed that the nodules develop at the beginning of oxidation in the steam containing environments, and do not increase in number with time, but only in size [36]. The high oxidation rate of the large precipitates in contact with the free surface could be thus expected to act as a local source of fast growing oxide, leading to a nodule, while the inner precipitates, having the same oxidation rate as the matrix, do not affect the corrosion at the outer surface.

4.2. SPP oxidation behaviour for the different alloys

The effect of size of the precipitates seems to be not the first parameter regarding their oxidation behaviour, this point is further discussed in this part. The examination of the oxidation state of SPP in binary alloys is not available at a microstructural level for the studies performed by authors [3–11], it is only available for Zr1%Nb, showing an 80 nm SPP unoxidised in the oxide [12]. The comparison of the present study is therefore only possible with these results. The size of the SPP is larger than those observed in the present study.

Yilmazbayhan et al. [29] observed β-Nb SPPs in Zirlo with a diameter of ∼80 nm unoxidised in the oxide. Bossis et al. observed a 50 nm unoxidised β-Nb SPP in the oxide [27] on Zr–1Nb–O.

In the case of alloys with ternary intermetallic SPPs present in the Zircaloys and other advanced zirconium alloys, unoxidised SPPs have been observed in several studies. These are summarized below for the different sizes observed:

- $Zr(Fe, Cr)_2$ of ∼0.8 μm by Kubo and Uno [37], smaller such SPPs are also observed by other authors [12,27,38,39].
- $Zr(Fe, V)_2$ of ∼200 nm by Pecheur [12].
- $Zr(Nb, Fe)_2$ of ∼100 nm by Park et al. [28].

In the study by Wadman et al. on Zr–0.5Sn–0.53Nb [40], the composition of the reported unoxidised SPPs in the oxide is not clearly stated, so it is not included in the above list.

From these data we conclude that the SPP size is not the major factor influencing the SPP oxidation state, as Nb-bearing SPPs reported in the present study are smaller than those observed by the authors mentioned above. Also ternary SPPs have been observed to remain unoxidised for the range of sizes smaller, similar or larger than those observed for Zr_3Fe and Zr_2Ni SPPs, in this study.

The oxidation behaviour of the SPP as revealed by FIB transverse sections and TEM samples can be subdivided into three cases:

(a) Alloys showing oxidation at the same time as the zirconium matrix and faster oxidation when in contact with the outer surface (see as an example Fig. 6a), this is the case of Zr_3Fe in Zr1%Fe and Zr_2Ni in Zr1%Ni.
(b) Alloys showing oxidation and diffusion of the alloying element to the outer surface; the case of the Zr–Fe alloys can be given as a clear example. It must be noted that even if this behaviour were present in other binary alloys, it is much slower than that for Zr1%Fe.
(c) Alloys showing delayed oxidation of the SPP with respect to the Zirconium matrix, this is the case of $ZrCr_2$ in Zr1%Cr and the ZrNb SPPs in Zr0.6%Nb.

For Zr_2Ni SPP Ploc observed a delayed oxidation with respect to the Zr-matrix [11] and an accelerated one for Zr_3Fe SPP while we observed both to behave fairly similar; accelerated with respect to the matrix if in contact with the outer surface and similar with respect to the matrix if not in contact with the outer surface. The preferential oxidation of the SPPs that are in contact with the outer surface at the metal–oxide interface is, however, not taking place in such a way, that they oxidise completely within a short time, as a small part having remained metallic could be observed for two of the three SPPs on Fig. 6a. We suggest therefore the term apparent acceleration, as the "rate" of oxidation of the SPP with respect to the matrix cannot be quantified in this study.

The presence of pure iron oxide at the outer surface of zirconium alloys has been reported by several authors before [11,13–15].

In the case of Zr–Cr and Zr–Ni binary alloys, such segregations have also been observed but to a much smaller extent [13]. The phenomenon has been observed at different temperatures and pressures; however the oxygen concentration in the steam seems to have an effect on this phenomenon [13].

On more complex alloys such as Zircaloy-4 Abolhassani et al. [15] found a layer of pure chromium oxide and underneath pure iron oxide layer on the surface of zirconia above oxidised $Zr(Fe, Cr)_2$ SPPs, after 1 h at 700 °C.

Iron oxide has also been observed on the surface of Zircaloy-2 by Auger [41] and by controlled potential reduction using a saturated Calomel electrode [13]. In the continuation of the present study the authors have also observed such segregations on Zircaloy-2 and the results will be reported in future publications.

The SPP in Zr1%Cr and Zr0.6%Nb exhibited lower oxygen concentrations than the surrounding oxide matrix, despite their much smaller sizes. To confirm this further, atom probe tomography can be applied. The crescent shaped cracks above the SPP facing the outer surface are observed both in the Zr1%Cr and Zr0.6%Nb. It must be noted that these cracks were not observed in the case of Zr1%Fe and Zr1%Ni. These cracks are the consequence of the delayed oxidation of the SPPs.

The presence of unoxidised [28,37–40] and partly oxidised [29] SPP with the hexagonal/face centred cubic $ZrCr_2$ structure has also been reported for oxides formed on Zircaloy-4 and crescent shaped cracks at the SPP-oxide interface facing the free oxidised surface can be observed on the micrographs presented in these papers [12,27–29,40]. As the applied preparation methods are different between our study and the previous works, and the milling direction in FIB was perpendicular to the cracks, these crescent shaped cracks are unlikely to be an artefact of the preparation process. The cause for their occurrence is probably the expansion of the oxidising Zr-matrix around the SPP containing Cr or Nb, before this latter starts to oxidise. The height of the cracks is in agreement with the volume difference between the Zr-matrix and the formed ZrO_2 expanding towards the outer surface, being dependent on the SPP size. Pecheur et al. have observed a large SPP in the oxide with a crack in Fig. 3a of Ref. [39]), supporting the above mentioned explanation for those cracks. The systematic presence of cracks at the interfaces of SPP within the oxide (e.g. Fig. 9b and c), on the free surface side, induced by the different P–B ratios and delayed oxidation, could be expected to be one of the possible nucleation sites for the larger cracks reported often in TEM observations [27–29]. This should to be investigated further to improve the understanding of the crack initiation and growth in the oxide scale on zirconium alloys.

The different oxidation behaviour of the SPP in the different alloys can have the following reasons:

- intrinsic oxidation behaviour of the alloying elements leads to different oxidation rates.
- different crystal structure of the SPP is at the origin of the differences.

A combination of the two factors presented above is likely to be responsible for the observed variation in SPP oxidation behaviour.

The $Zr(Fe, Cr)_2$ SPPs present in Zircaloy-2 and Zircaloy-4 have the same structure as the $ZrCr_2$ SPPs and also their alloying element content is similar, but their chromium content is lower.

The $Zr_2(Fe, Ni)$ SPPs also contained in Zircaloy-2 have not been reported to be unoxidised in the oxide [37], with the average SPP size being 0.47 µm for both SPP types present in Zircaloy-2. So only the SPPs containing Cr and having the structure typical for the $ZrCr_2$ SPPs have been observed unoxidised in the Zircaloys.

In the oxide formed on Zr1%Fe and Zr1%Ni we have not observed small SPPs with the typical crack associated to unoxidised SPPs. As the SPP distribution and their size is not homogeneous in Zr1%Fe and Zr1%Ni, it could be that no small SPPs containing Fe or Ni in the same size range as the Cr or Nb containing SPPs were present in the oxide (they correspond to more than 30% of the whole SPP population in Zr1%Fe), however this is not very likely. The SPPs which had remained unoxidised should have been observed due to the crack associated with them if they were present, which was not the case during thorough scanning of the oxide.

Therefore the nature of the SPP (alloying element and crystal structure) seems to be a more plausible parameter as opposed to the SPP size; the alloying elements such as Cr, Nb, and V are reported to lead to unoxidised SPP on zirconium based alloys [12,27–29,37–40,42].

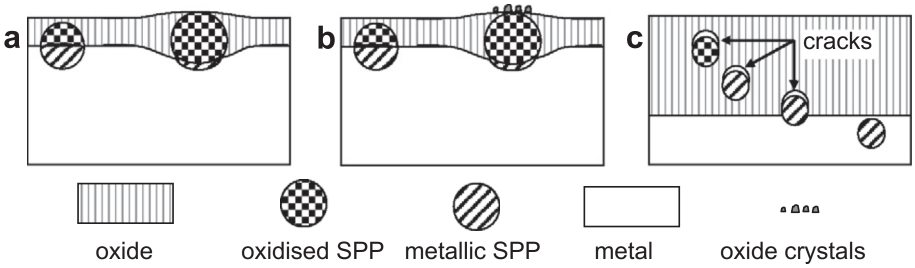

Fig. 12. Schematic view of the metal–oxide interface and the oxidation state of the SPP. (a) SPP oxidation behaviour observed for Zr_3Fe and Zr_2Ni SPP, (b) oxide crystal formation as observed for Zr_3Fe, and (c) SPP oxidation behaviour observed for $ZrCr_2$ and Zr/Nb SPP.

The oxidation tendency observed for SPP not in contact with the outer surface is: $Zr_3Fe \approx Zr_2Ni \approx$ Zr-matrix > Zr/Nb SPP > $ZrCr_2$, also shown schematically in Fig. 12. As mentioned above, the behaviour is classified into the three following categories:

(a) For the alloys Zr1%Fe and Zr1%Ni, SPPs in contact with the outer surface show an apparent faster oxidation rate with respect to the zirconium matrix resulting in an oxide protrusion at the surface and an undulated metal–oxide interface. This behaviour could be connected to the nucleation process of nodules. SPPs not in contact with the outer surface oxidise at approximately the same rate as the surrounding zirconium matrix (Zr_3Fe and Zr_2Ni).
(b) Alloying elements diffuse to the outer surface and form pure oxides (Zr1%Fe).
(c) For the alloys Zr1%Cr and Zr0.6%Nb, SPPs oxidise after the matrix and once fully surrounded by the oxide at a distance from the interface (Zr/Nb SPP and $ZrCr_2$).

Binary alloys are not usually used in the reactor; and more often ternary alloys or more complex alloys are used. Therefore the SPP of these alloys are often ternary intermetallics.

Currently used alloys in nuclear power plants contain SPPs exhibiting a delayed oxidation with respect to the zirconium matrix [12,27–29,37–40,42], with the exception of the $Zr_2(Fe, Ni)$ SPPs in Zircaloy-2, for which this behaviour has not been reported [37]. Therefore a correlation between delayed oxidation and improved corrosion performance should be studied in detail, as all Zircaloys and the Nb-containing alloys contain SPPs showing delayed oxidation.

The impact of the delayed oxidation of the SPP on the time to oxide breakdown is of interest for the commercial alloys used in nuclear power plants, as they contain these SPP types. Work is in progress to further investigate this phenomenon.

5. Conclusions

The in situ oxidation at 415 °C revealed the formation of specific oxide protrusions at the surface corresponding to the oxidised SPP of Zr1%Fe and Zr1%Ni. For Zr1%Cr, Zr0.6%Nb, and pure Zr the protrusions are either not existing or they are too small to be unambiguously distinguished from the matrix oxide grains on the surface.

The oxidation tendency observed for SPP at the metal–oxide interface not in contact with the outer surface is: $Zr_3Fe \approx Zr_2Ni \approx$ Zr-matrix > ZrNb SPP > $ZrCr_2$, also shown schematically in Fig. 12. In the case of Zr_3Fe, diffusion of Fe to the free surface and formation of pure iron oxide crystals is observed.

The similar oxidation of the SPP containing iron or nickel, in contrast to the delayed oxidation of Cr and Nb containing SPP at the initial stage of oxidation with respect to the Zr-matrix is interesting concerning the overall corrosion properties of these alloys. Their locally dissimilar behaviour does not seem to be correlated to their short and mid-term corrosion performance observed in the autoclave after 3 and 110 days by Barberis et al. [4]. The reason for the similar global oxidation behaviour at distinctly different SPP oxidation is important to be clarified. The observations made during the initial stages of the oxidation prove that the nature of the alloying element affects the behaviour of the SPP during the first hours of oxidation in a significant way.

In this study, the chemistry and the size of the precipitates were changing simultaneously. It was, however, possible to draw conclusions on the effects of sizes and locations of the precipitates on the mechanisms of oxidations of these precipitates. In order to expand these conclusions and improve our understanding of the role of the precipitates on the corrosion mechanisms of Zr-alloys, similar experiments are planed with alloys processed in such a way that precipitate sizes would be similar for all the alloys. In that case it would be expected that larger size of $ZrCr_2$ and ZrNb precipitates would not affect the oxidation behaviour of these SPPs.

Acknowledgements

The authors acknowledge the provision of the autoclaved binary alloys by P. Barberis from CEZUS Research Centre, Ugine/France. M. Leboeuf from SMN, University of Neuchâtel, is acknowledged for help with ESEM and AFM studies. Mrs. J. Krbanjevic is thanked for assistance with FIB TEM sample preparation. This project is partly financed by Swiss*nuclear*.

References

[1] T. Isobe, T. Murai, Y. Mae, ASTM STP 1295 (1996) 203–217.
[2] H. Beie, A. Mitwalski, F. Garzarolli, H. Ruhmann, ASTM STP 1245 (1993) 615–643.
[3] M. Harada, M. Kimpara, K. Abe, ASTM STP 1132 (1991) 368–391.
[4] P. Barberis, E. Ahlberg, D. Charquet, C. Lemaignan, G. Wikmark, M. Dahlbäck, M. Limbäck, P. Tägström, B. Lehtinen, ASTM STP 1423 (2002) 33–55.
[5] P. Barberis, B. Baroux, La Revue de Metallurgie-CIT/Science et Genie des Materiaux (2000) 689–698.
[6] D.R. Lutz, S.B. Wisner, D.M. Farkas, R.B. Adamson, in: Top Fuel 99, Avignon, France, 1999.
[7] T. Murai, T. Isobe, Y. Takizawa, Y. Mae, ASTM STP 1354 (2000) 623–640.
[8] T. Kondo, T. Kimura, J. Nucl. Mater. 41 (1971) 121–132.
[9] L. Kumar, D.D. Sarma, S. Krummacher, Appl. Surf. Sci. 32 (1988) 309–319.
[10] E.A. Gulbransen, K.F. Andrew, Corrosion 23 (1967) 231–235.
[11] R.A. Ploc, ASTM STP 1023 (1988) 498–514.
[12] D. Pecheur, J. Nucl. Mater. 278 (2000) 195–201.
[13] P.J. Shirvington, J. Nucl. Mater. 37 (1970) 177–202.
[14] N. Ramasubramanian, J. Nucl. Mater. 55 (1975) 134–154.
[15] S. Abolhassani, M.M. Dadras, M. Leboeuf, D. Gavillet, J. Nucl. Mater. 321 (2003) 70–77.
[16] A. Grandjean, Y. Serruys, J. Nucl. Mater. 273 (1999) 111–115.
[17] M. Inagaki, M. Kanno, H. Maki, ASTM STP 1132 (1991) 437–460.
[18] A. Yilmazbayhan, A.T. Motta, R.J. Comstock, G.P. Sabol, B. Lai, Z. Cai, J. Nucl. Mater. 324 (2004) 6–22.
[19] J. Lin, H. Li, J.A. Szpunar, R. Bordoni, A.M. Olmedo, M. Villegas, A.J.G. Maroto, Mater. Sci. Eng. A 381 (2004) 104–112.
[20] C. Roy, B. Burgess, Oxid. Met. 2 (1970) 235–261.
[21] J. Godlewski, ASTM STP 1245 (1994) 663–686.
[22] B. Cox, J. Corros. Sci. Eng. 6 (2003).
[23] H. Anada, K. Takeda, S. Hagi, T. Murata, A. Oe, T. Miyashita, in: Proceedings of the ANS International Topical Meeting on LWR Fuel Performance, IAEA, Park City, 2000, pp. 445–456.
[24] S. Kass, ASTM STP 368 (1964) 3–27.
[25] B. Cox, Y.M. Wong, J. Nucl. Mater. 270 (1999) 134–146.
[26] S. Abolhassani, R. Restani, T. Rebac, F. Groeschel, W. Hoffelner, G. Bart, W. Goll, F. Aeschbach, ASTM STP 1467 (2006) 467–493.
[27] P. Bossis, J. Thomazet, F. Lefebvre, ASTM STP 1423 (2002) 190–221.
[28] J.-Y. Park, S.J. Yoo, B.-K. Choi, Y.H. Jeong, J. Alloys Compd. 437 (2007) 274–279.
[29] A. Yilmazbayhan, E. Breval, A.T. Motta, R.J. Comstock, J. Nucl. Mater. 349 (2006) 265–281.
[30] W. Wang, S. Abolhassani, M.M. Dadras, C. Lemaignan, in preparation.
[31] F. Czerwinski, J.A. Szpunar, Corros. Sci. 39 (1997) 147–158.
[32] G. Binnig, C.F. Quate, C. Gerber, Phys. Rev. Lett. 56 (1986) 930–933.
[33] D. Drouin, A.R. Couture, D. Joly, X. Tastet, V. Aimez, R. Gauvin, Scanning 29 (2007) 92–101.
[34] N.B. Pilling, R.E. Bedworth, J. Inst. Met. 29 (1923) 529–582.
[35] C.H. Xu, W. Gao, Mater. Res. Innov. 3 (2000) 231–235.
[36] P. Rudling, G. Wikmark, J. Nucl. Mater. 265 (1999) 44–59.
[37] T. Kubo, M. Uno, ASTM STP 1132 (1991) 476–498.
[38] E.R. Bradley, R.A. Perkins, Characterisation of Zircaloy corrosion films by analytical transmission electron microscopy, in: Fundamental Aspects of Corrosion of Zirconium Base Alloys in Water Reactor Environments, IWGFPT/34 IAEA, Vienna, 1990, pp. 101–106.
[39] D. Pecheur, F. Lefebvre, A.T. Motta, C. Lemaignan, J.F. Wadier, J. Nucl. Mater. 189 (1992) 318–332.
[40] B. Wadman, Z. Lai, H.-O. Andrén, A.-L. Nyström, P. Rudling, H. Pettersson, ASTM STP 1245 (1994) 579.
[41] Y. Hatano, M. Sugisaki, J. Nucl. Sci. Technol. 33 (1996) 829–833.
[42] D. Pecheur, F. Lefebvre, A.T. Motta, C. Lemaignan, D. Charquet, ASTM STP 1245 (1994) 687–708.